Diamond & Related Materials 137 (2023) 110091

Contents lists available at ScienceDirect

Diamond & Related Materials

journal homepage: www.elsevier.com/locate/diamond

Optimized unidirectional and angle-insensitive ultra-broadband absorber based on layered graphene photonic structure

Zhao Tang, Jie Xu, Shuo Wang, Hai-Feng Zhang *

College of Electronic and Optical Engineering & College of Flexible Electronics (Future Technology), Nanjing University of Posts and Telecommunications (NJUPT), Nanjing 210023, PR China

ARTICLE INFO

Keywords:
Non-reciprocal ultra-wide absorber
Angular stability
Terahertz
Graphene
Chaotic gray wolf optimization

ABSTRACT

Using a chaotic gray wolf optimization algorithm to drive the transfer matrix method, a nonreciprocal and angle-insensitive absorber with ultra-wide bandwidth absorption is realized in a layered photonic structure comprised of graphene, which is spliced of a periodic sequence and a quasi-periodic sequence on a normalized scale. Compared to the periodic sequence, the proposed cascading construction has more preponderance in terms of bandwidth and angular stability. The surface conductivity of the graphene layer, which manipulates the absorption effect, can be modulated by the Fermi level, causing the characteristics of the proposed absorber tuned. The Fermi level of graphene, dielectric constants, and thicknesses of ordinary media, are optimized by the chaotic gray wolf algorithm, contributing to the decent improvement of absorption with a relative bandwidth of up to 127 %. Most importantly, in the 1.5–4.5 THz, the angular stability reaches 86° under the TM mode and 70° in TE one. The impacts of sequence number N of periodic sequence and M of quasi-periodic sequence on absorption in both angle and frequency domains are investigated. Additionally, the impedance match theory is introduced to express excellent absorption performance.

1. Introduction

To address the increasingly complex electromagnetic environment, there is a growing demand for ultra-wideband, wide-angle, and angle-insensitive absorbers in areas such as military stealth [1,2], wireless communication [3], security detection, and protection [4,5]. In recent years, several promising metamaterial absorbers have emerged. For instance, Baqir et al. [6] proposed a nanostructured hyperbolic metamaterial absorber that exhibits near-perfect absorption in the ultraviolet frequency range. However, this absorber is highly sensitive to the incident angle. Subsequently, in 2020, a gallium-doped zinc oxide (GZO) nanowire-based metamaterial absorber was introduced, achieving broadband and wide-angle absorption in the near-infrared and short-wave infrared regions [7]. Nevertheless, further improvements are required in terms of relative bandwidth (*RBW*) and angle stability. Furthermore, there have been numerous studies on absorbers operating in this frequency range. In a subsequent development in 2021, a novel metamaterial absorber composed of a quadruple symmetric square fractal structure was devised, which exhibited polarization-insensitive and dual-band absorption characteristics [8]. However, the bandwidth achieved at the normal incidence was limited to 9.5–10.55 THz and 12.3–13.35 THz, entailing further improvement in its absolute bandwidth (*AB*).

Graphene has emerged as a highly attractive two-dimensional material for optoelectronic devices owing to its wide spectral range and exceptionally high carrier mobility [9], which shows tremendous potential for producing saturable absorbers [10–12], light modulators [13], transparent electrodes [14–16], and solar cells [17,18]. However, the absorption efficiency of single-layer graphene is meager, reaching only 2.3 % in the visible and near-infrared regions [19], which impedes the design of optical detectors. It is noteworthy that the layered photonic structure (LPS) embedded with graphene sheets can manifest some peculiar phenomena, including multi-channel [20–22], single-frequency [23], and single-peak absorption [24–27]. This has sparked the interest of numerous scholars, leading to many studies that explore the integration of graphene layers into isotropic one-dimensional layered photonic structures. However, despite numerous types of research aiming to improve the absorption performance of graphene-incorporated LPS, the absence of systematic design methods often leads to suboptimal choices of parameters and structural adjustments. Consequently, the effective absorption bandwidth and angular stability of graphene in previous studies require further improvements. Additionally, it is worth noting

* Corresponding author.
E-mail address: hanlor@njupt.edu.cn (H.-F. Zhang).

https://doi.org/10.1016/j.diamond.2023.110091
Received 16 April 2023; Received in revised form 30 May 2023; Accepted 2 June 2023
Available online 5 June 2023

that the significant value of non-reciprocity has been largely overlooked in most prior investigations of absorbers, resulting in relatively limited research on absorbers with non-reciprocal properties.

To design an absorber with superior absorption bandwidth, and angle stability, and achieve impeccable non-reciprocal functionality, an enhanced variant of the gray wolf optimization (GWO) algorithm has been implemented to optimize the parameters of the suggested cascading configuration. GWO, devised by Mirjalili *et al* [28], represents a cutting-edge intelligent optimization algorithm that has garnered widespread attention in the realm of intelligent evolutionary algorithms owing to its robustness, rapid convergence speed, and minimal parameter requisites. However, when confronted with high-dimensional and intricate optical quandaries, conventional GWO often exhibits a proclivity towards local optima convergence. To surmount this challenge, the present research incorporates the chaotic gray wolf optimization (CGWO) algorithm, which effectively capitalizes on the exploratory, regularity, and stochastic attributes of chaos to substantially enhance the convergence quality of the algorithm.

In this paper, the CGWO has been utilized to propel the transmission matrix method [29], to design a non-reciprocal absorber that exhibits ultra-wide bandwidth absorption with decent angular stability. Additionally, the physical impact of the principal parameters has been examined, and the impedance matching theory has been presented to verify the effectiveness of the CGWO. We believe that the proposed non-reciprocal absorber holds immense practical value in various domains such as stealth technology, energy harvesting, and beyond.

2. Model and theory

2.1. Schematic structure

The cascading structure, composed of periodic and quasi-periodic sequences in an air environment, is illustrated in Fig. 1. The positive direction of the z-axis signifies the forward propagation of electromagnetic waves (EMs), while the negative direction along the z-axis denotes the backward propagation. The periodic part is composed of materials A, C, and graphene layer G, arranged in the sequence $\{AGC\}^N$ (where N is the number of periods). On the other hand, the quasi-periodic part is composed of the symmetrical and recursive Octonacci or Thue-morse sequences [30,31], with air layer B and graphene layer G.

In the Octonacci sequence, the initial parameters are $Oct_0 = \{BGB\}$ and $Oct_1 = \{GBG\}$, represented as a light green square, and a dark green square in Fig. 1, respectively. The sequence then follows the rule $Oct_M = Oct_{M-1}Oct_{M-2}Oct_{M-1}$. The Thue-morse sequence has a recurrence rule where '0' in the nth term becomes '01' in the $n + 1$th term and '1' becomes '10', with '0' represented by {BGB} and '1' represented by

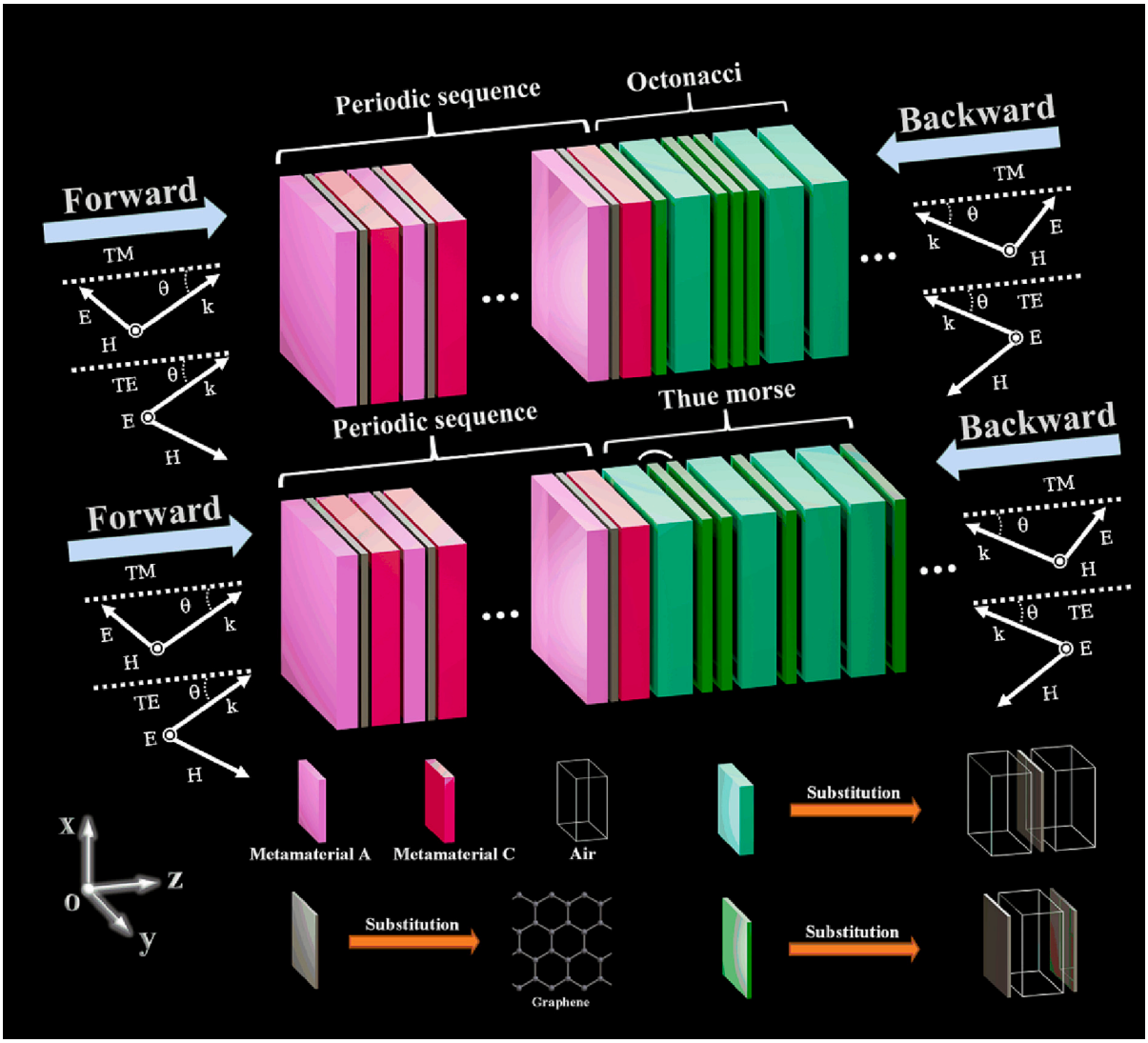

Fig. 1. A schematic representation of composite structures consisting of a periodic sequence and a quasi-periodic sequence.

{GBG}.

In this model, the thickness and relative dielectric constants of materials A and C are totally determined artificially, which are expressed as d_a, d_c, ε_a, ε_c respectively. Also, the thickness of the air layer (model B) is optimized, expressed as d_b.

2.2. Theory of computation

Graphene is highly suitable for supporting surface plasmon excitations of terahertz (THz) waves, making it a compelling candidate for THz absorbers. By modulating the Fermi level of graphene through voltage or chemical doping, the carrier concentration, resonance frequency, and absorption rate can be controlled, greatly broadening the optimization space for graphene-based absorption effects. As a frequency-dependent medium, the conductivity of the graphene sheet can be calculated according to the Kubo formula [32,33].

$$\sigma_g = \sigma_g^{inter} + \sigma_g^{intra} \tag{1}$$

In Eq. (1) σ_g^{inter} is the inter-band conductivity, and σ_g^{intra} is the intra-band conductivity. The calculation formulas of them respectively are in Eqs. (2) and (3)

$$\sigma_g^{intra} = \frac{ie^2 k_B T}{\hbar^2 \pi(\omega + i/\tau)} \left(\frac{\mu_c}{k_B T} + 2ln\left(e^{\frac{-\mu_c}{k_B T}} + 1\right) \right) \tag{2}$$

$$\sigma_g^{inter} = i\frac{e^2}{4\pi\hbar} ln\left|\frac{2\mu_c - \hbar(\omega + i/\tau)}{2\mu_c - \hbar(\omega + i/\tau)}\right| \tag{3}$$

where e represents the electric charge of electrons, k_B represents the Boltzmann constant, and $T = 300$ K is the ambient temperature. In addition, ħ denotes the reduced Planck constant, ω represents the circular frequency of the EMs, and τ represents the phenomenological scattering rate (with $\tau = 10^{-13}$s). The Fermi level of graphene (denoted as μ_c) is optimized between 0.1 and 1 eV. Provided that the electronic band structure of the graphene film is not affected by the environment, its effective dielectric constant ε_g can be calculated from Eq. (4)

$$\varepsilon_g = 1 + i\sigma_g / \omega\varepsilon_0 d_g \tag{4}$$

where ε_0 is the vacuum permittivity, and $d_g = 0.34$ nm is the thickness of the graphene layer.

In order to examine the dispersion relations and transmission properties of THz waves propagating through the LPS, the transmission matrix method [29] is employed, which is based on Maxwell's equations and derived from iterative equations of the electric and magnetic fields that satisfy continuous boundary conditions for both fields.

The transfer matrix of the ith layer of the medium in the model is

$$\boldsymbol{M}_i = \begin{bmatrix} cos\delta_i & -\frac{j}{\eta_i} sin\delta_i \\ -j\eta_i sin\delta_i & cos\delta_i \end{bmatrix}, (i = A, B, C, G) \tag{5}$$

In Eq. (5), the thicknesses, relative dielectric constants of the materials, and incident angle of ith media respectively are d_i, ε_i (parameters to be optimized) and θ_i. η_i represents the admittance of the ith layer, and δ_i is the phase of the ith layer. The phase can be calculated from Eq. (6).

$$\delta_i = \left(\frac{\omega}{c}\right) \sqrt{\varepsilon_i} d_i cos\theta_i \tag{6}$$

When an EM is in the transverse electric (TE) polarization, the admittance can be calculated by Eq. (7)

$$\eta_i = \sqrt{\frac{\varepsilon_0}{\mu_0}} \sqrt{\varepsilon_i} cos\theta_i \tag{7}$$

In the transverse magnetic (TM) polarization, it follows Eq. (8)

$$\eta_i = \sqrt{\frac{\varepsilon_0}{\mu_0}} \frac{\sqrt{\varepsilon_i}}{cos\theta_i} \tag{8}$$

For the periodic part $(AGC)^N$, the overall transmission matrix can be expressed as Eq. (9)

$$\boldsymbol{M}_{periodic} = (\boldsymbol{M}_A \boldsymbol{M}_G \boldsymbol{M}_C)^N \tag{9}$$

The transfer matrix for quasi-periodic sequences, such as the Octonacci and Thue-morse sequences, can be calculated using the following Eq. (10)

$$\begin{cases} \boldsymbol{M}_{Octonacci} = \boldsymbol{M}_E \boldsymbol{M}_D \boldsymbol{M}_E \boldsymbol{M}_E \boldsymbol{M}_E \cdots \\ \boldsymbol{M}_{Thue\text{-}morse} = \boldsymbol{M}_D \boldsymbol{M}_E \boldsymbol{M}_E \boldsymbol{M}_D \boldsymbol{M}_E \cdots \end{cases} \tag{10}$$

The transmission matrix of the whole structure is indicated in Eq. (11)

$$\boldsymbol{M} = \prod_{i=1}^{N} \boldsymbol{M}_i = \boldsymbol{M}\text{periodic} \cdot \boldsymbol{M}\text{quasi-periodicity} = \begin{bmatrix} m_{11} & m_{12} \\ m_{21} & m_{22} \end{bmatrix} \tag{11}$$

By Eq. (11), the transmittance and reflectance of EMs passing through the structure can be calculated in Eq. (12)

$$\begin{cases} t = \dfrac{2\eta_0}{m_{11}\eta_0 + m_{12}\eta_0\eta_{N+1} + m_{21} + m_{22}\eta_{N+1}} \\ r = \dfrac{m_{11}\eta_0 + m_{12}\eta_0\eta_{N+1} - m_{21} - m_{22}\eta_{N+1}}{m_{11}\eta_0 + m_{12}\eta_0\eta_{N+1} + m_{21} + m_{22}\eta_{N+1}} \end{cases} \tag{12}$$

Since the entire structure is in air, $\eta_0 = \eta_{N+1}$, and the absorptance A can be written as

$$A = 1 - |t|^2 - |r|^2 \tag{13}$$

By using the method described above, the absorption rates of forward and backward-propagating EMs can be easily obtained.

GWO is a novel intelligent optimization algorithm, that simulates the phenomenon of wolf hunting for modeling. The hunted prey is the optimal solution, and the location coordinates of the wolves donate the values of the parameters to be optimized. Similar to the hierarchical leadership system of wolves, the algorithm specifies that the optimal solution after each iteration is the king of wolves, codenamed α, the solutions ranked second and third in fitness are codenamed β and γ, respectively, and the remaining solutions are ψ. α is responsible for leading the wolf pack forward (guiding the direction of the next iteration), β and γ assist the king, and the ψ follows the leadership.

The algorithm firstly initializes the positions of each wolf (corresponding to a fitness value), then the algorithm starts iterating and the wolves start searching for prey (towards a more optimal solution), each iteration can be represented by the following equations

$$\boldsymbol{D} = |\boldsymbol{C} \times \boldsymbol{X}p(s) - \boldsymbol{X}(s)| \tag{14}$$

$$\begin{cases} \boldsymbol{X}1 = \boldsymbol{X}\alpha - \boldsymbol{B}1 \times \boldsymbol{D}\alpha \\ \boldsymbol{X}2 = \boldsymbol{X}\beta - \boldsymbol{B}2 \times \boldsymbol{D}\beta \\ \boldsymbol{X}3 = \boldsymbol{X}\gamma - \boldsymbol{B}3 \times \boldsymbol{D}\gamma \end{cases} \tag{15}$$

Eq. (14) is responsible for calculating the distance between the prey and the wolves after each iteration, and the position of the wolves after the next iteration is calculated in Eq. (15).

$\boldsymbol{D}$ represents the distance between the prey and the gray wolf, $\boldsymbol{X}_p(s)$ displays the position coordinate of the prey, $\boldsymbol{X}(s)$ is the position coordinates of the gray wolf, and s is the number of iterations. $\boldsymbol{B}$ and $\boldsymbol{C}$ are the coefficient vectors.

After encircling the prey, the three wolves α, β and γ guide the other wolves to update their positions and start attacking the prey with the following Eqs. (16) and (17)

$$\begin{cases} \boldsymbol{D}_\alpha = |\boldsymbol{C}_1 \times \boldsymbol{X}_\alpha - \boldsymbol{X}| \\ \boldsymbol{D}_\beta = |\boldsymbol{C}_2 \times \boldsymbol{X}_\beta - \boldsymbol{X}| \\ \boldsymbol{D}\gamma = |\boldsymbol{C}_3 \times \boldsymbol{X}_\gamma - \boldsymbol{X}| \end{cases} \tag{16}$$

$$\begin{cases} \boldsymbol{X}1 = \boldsymbol{X}\alpha - \boldsymbol{B}1 \times \boldsymbol{D}\alpha \\ \boldsymbol{X}2 = \boldsymbol{X}\beta - \boldsymbol{B}2 \times \boldsymbol{D}\beta \\ \boldsymbol{X}3 = \boldsymbol{X}\gamma - \boldsymbol{B}3 \times \boldsymbol{D}\gamma \end{cases} \tag{17}$$

where $\boldsymbol{D}_{\alpha}$, $\boldsymbol{D}_{\beta}$, and $\boldsymbol{D}_{\gamma}$ denote the distances between the common wolf to α, β and γ, respectively. $\boldsymbol{X}_{\alpha}$, $\boldsymbol{X}_{\beta}$, and $\boldsymbol{X}_{\gamma}$ represent the positions of α, β, and γ, respectively. $\boldsymbol{X}$ is the current position of the wolf. And $\boldsymbol{X}_1$, $\boldsymbol{X}_2$, and $\boldsymbol{X}_3$ are the direction and step length of the current wolf towards α, β, and γ, respectively. Finally, the updated position of this wolf is obtained by Eq. (18)

$$|\boldsymbol{A}| \tag{18}$$

where the location of this wolf after the update is $\boldsymbol{X}(t+1)$.

The fluctuation range of $\boldsymbol{B}$ in the formula decreases during the iteration, while the mode of $\boldsymbol{B}$ determines the behavior of the gray wolf. When $|\boldsymbol{B}| > 1$, the gray wolf moves away from the prey and continues to search for a better solution globally. However, when $|\boldsymbol{B}| < 1$, the gray wolf approaches the prey and initiates an attack.

For $\boldsymbol{C}$, due to its random value between [0,2], it indicates the random influence weight of wolf location on prey. Due to the randomness of $\boldsymbol{C}$, it enables GWO to effectively jump out of the local optimal solution and keep searching for the optimal solution within the global range.

However, similar to other swarm intelligence algorithms, standard GWO also has the disadvantages of easily falling into local optimum, slow convergence speed in the later stage, and low solution accuracy. With the help of the randomness, ergodic and regular characteristics of chaos, CGWO uses logistic chaotic mapping to generate sequences to iterate the positions wolf pack, making individuals of the population use the information of the solution space as much as possible, which greatly improves the search efficiency and the ability of global search the algorithm. Based on the above analysis, chaos theory is introduced into the position update Eq. (18) of GWO, and the improved position update as Eq. (19) is obtained

$$\boldsymbol{X}(t+1) = \frac{1}{3}\sum_{i=1}^{3}(\boldsymbol{X}_i - R_n \cdot (R' \cdot \boldsymbol{X}_i - \boldsymbol{X}_i)) \tag{19}$$

where R_n and $R_n^{'}$ is the vector of chaotic maps.

In the objective function, the parameters to be optimized are separately the permittivities ε_a and ε_c for media A and C, whose optimal ranges are 1–100, the thickness d_a, d_c, and d_b for A, C, and air layer B with the optimization range 1–100 μm. The last parameter is the Fermi level μ_c (0.1–1 eV) of graphene. Finally, the logical flow chart of the optimization is shown in Fig. 2.

3. Results and discussion

3.1. Nonreciprocal and ultra-wide bandwidth absorption after optimization

To achieve nonreciprocal and ultra-broad band absorption at normal incidence, the CGWO is used to optimize the structure within 0.1–10 THz with the *AB* as the objective function.

Given the discrete nature of variables *N* and *M* as positive integers, while the search space of CGWO consists of continuous values, the direct optimization of *N* and *M* within CGWO is not feasible. Instead, the enumeration method is employed to determine the values of them. This approach not only significantly reduces the computational complexity of CGWO but also provides an opportunity to observe the influence of different values of *N* and *M* on the absorption.

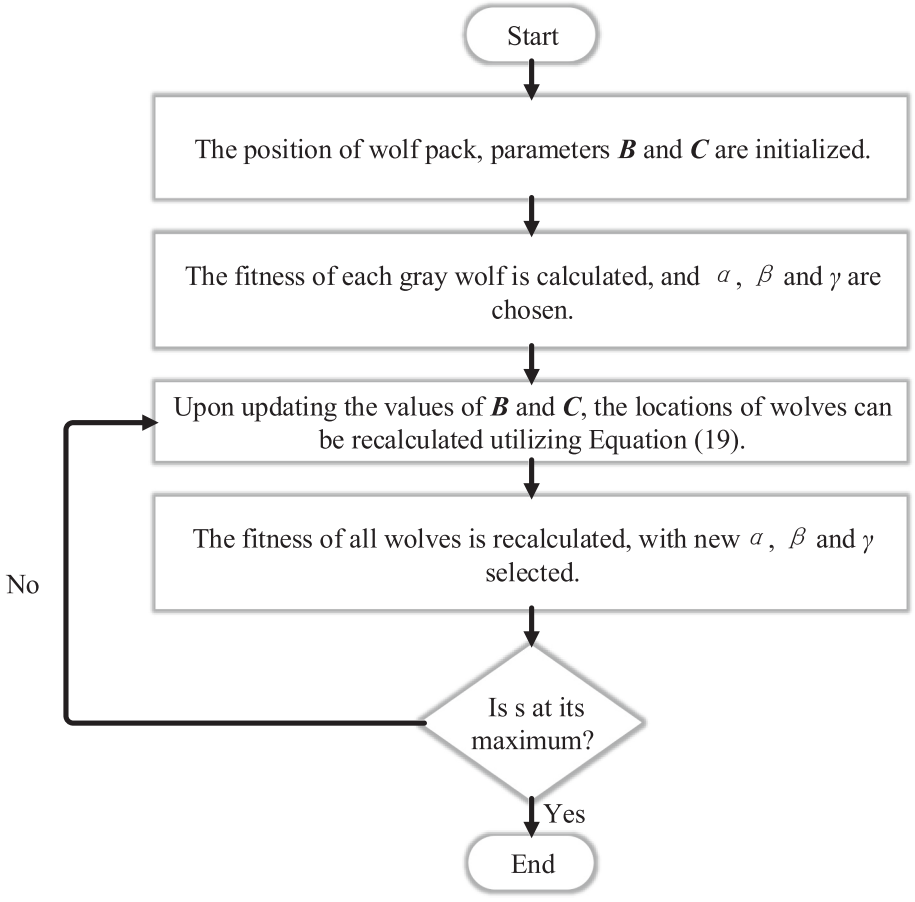

Fig. 2. Algorithm process of CGWO.

3.1.1. Effect of N on the absorption

With the Octonacci 6 (Oct_6) and Thue-morse 6 (Thu_6) as the quasi-periodic sequences, and N increasing linearly, the impacts of N on the absorption results and the optimized parameters are presented in Table 1. As N varies from 1 to 5, it can be observed that the nonreciprocal AB with Thu_6 as the quasi-period sequence fluctuates between 7.4 THz and 7.5 THz, with the RBW consistently above 120 %. Specifically, the minimum RBW of 120.97 % is achieved at $N = 5$, while the maximum RBW of 127.12 % is obtained at $N = 1$. Meanwhile, for the Oct_6 implanted structure, AB exhibits fluctuation within the range of 7.6–7.81 THz. The minimum RBW value is observed at $N = 1$ or 6, at 122.58 %, while the maximum RBW value is obtained at $N = 2$, at 128.98 %.

The perfect non-reciprocity of the absorber is achieved through the disruption of the symmetry of its topological structure. For EMs propagating along the positive z-axis, they first pass through a periodic structure $\{AGC\}^N$. Due to the significant refractive index difference between the optimized media A and C, the EMs transition from an optically dense medium to an optically rare medium. When the incident angle exceeds a certain angle (critical angle), a large portion of the forward-propagating EMs is reflected. On the other hand, EMs propagating in the opposite direction along the negative z-axis initially traverse a quasi-periodic structure composed of graphene layers and air layers, where they are extensively absorbed by the electrons in graphene. Consequently, the overall behavior of this structure is characterized by a substantial reflection of forward-propagating EMs and significant absorption of backward-propagating EMs, thereby achieving the perfect non-reciprocal absorption characteristics.

It is evident that the change of N has little effect on absorption. There are two reasons for these results. Firstly, the resonant structure of the periodic part produces far fewer absorption peaks than the quasi-periodic structure because of the smaller number of plies. Secondly, the absorption peaks generated by both periodic and quasi-periodic sequences have overlapping parts. Thus, the change of N does not significantly improve the absorption. Therefore, the only role of the periodic part is to implement non-reciprocity caused by its asymmetry.

Furthermore, as shown in Table 1, it is apparent that the absorption bandwidth is marginally enhanced when Oct_6 is employed as the quasi-periodic series in contrast to using Thu_6. This is attributed to the significant number of photonic structural layers that conceal the absorption variations caused by spatial disparities between the two quasi-periodic sequences. Thus, it can be anticipated that as M diminishes, the difference in absorption outcomes between the two structures will be more pronounced, a phenomenon that will be demonstrated in the ensuing analysis.

Since the absorption effect is better when Oct6 is used as the quasi-periodic sequence, and the fluctuation of N has less influence on the absorption, the selection of Oct_6 as the sole quasi-periodic sequence is justified. To facilitate expeditious analysis, the results of the non-reciprocal ultra-wide-band optimization, spanning a wide frequency span of 0.1–10 THz, for three different $N = 2$, 3, and 4, are presented in Fig. 3.

In Fig. 3, the two gray dashed lines correspond to absorption rates of 0.9 and 0.1, respectively. A frequency band that meets the non-reciprocal criteria, with forward propagation absorption rate below 0.1 and backward propagation absorption rate exceeding 0.9, is marked by blue diagonals to indicate an ideal absorption band.

At $N = 2$, as shown in Fig. 3(a), RBW reaches its maximum value of 129.04 % with a low cutoff frequency of 2.15 THz and an upper cutoff frequency of 9.97 THz, resulting in ultra-wide band absorption. As N increases to 3 and 4, as seen in Fig. 3(b) and (c), the lower cutoff frequency rises from 2.31 THz to 2.37 THz, while the upper cutoff frequency remains fixed at 10 THz, resulting in AB of 7.69 THz and 7.63 THz and RBW of 125.14 % and 123.76 %, respectively. Moreover, for the absorption curve of EMs in forward propagation, there are only two peaks at 0.25 THz and 1.57 THz for $N = 2$, whereas when $N = 3$, three peaks appear at 0.32 THz, 1.24 THz, and 2.06 THz, and when $N = 4$, four peaks arise at 0.26 THz, 0.97 THz, 1.73 THz, and 2.21 THz. The rise in the number of peaks can account for the reduction of the non-reciprocal absorption AB as N increases.

As for the absorption curve of the back-propagating EMs, when $N = 2$, there are three troughs at 3.97 THz, 7.33 THz, and 8.89 THz, and all of them experience a redshift with the increase of N. With the aid of CGWO, the absorption rates at all three troughs are optimized to be >0.9, realizing ultra-wide bandwidth absorption.

By observing the illustration, it is clear that the excellent non-reciprocal absorption band stabilizes around 2.5 to 10 THz as N increases, while the optimization in the 0.1 to 2.5 THz is always less than ideal. At the same time, in the 0.1–2.5 THz, the oscillation of the absorption curve of forward propagation increases with the increase of the N value. It can be predicted that even if the number of periodic structure layers continues to rise, the 0.1–2.5 THz is still tough to be optimized when the total optimization domain is still 0.1–10 THz, which is because the impedance matching in this band is out of balance, and the resonant frequency of the structure does not match the EMs. To sum up, the optimization in the overall range of 0.1–10 THz has little potential to obtain the ideal effect in the band of 0.1–2.5 THz. Therefore, consider changing the range condition of the objective function to reduce the total range of optimization. The 0.1–3 THz is separately optimized, with $N = 2$ and taking Thu_6 and Oct_6 as the quasi-periodic sequences, and the results are as follows.

The absorption outcomes within the 0.1–3 THz are illustrated in Fig. 4. In Fig. 4(a), using Thu_6 as the quasi-periodic sequence, with ε_a amounting to 1, d_a measuring 39.547 μm, d_b registering 31.632 μm, ε_c equating to 100, d_c measuring 4.247 μm, and μ_c is 0.025 eV. In Fig. 4(b), taking Oct6 as the quasi-periodic sequence, with ε_a is 100, d_a measuring 4.207 μm, d_b measuring 27.58 μm, ε_c amounting to 1, d_c registering 39.662 μm, and μ_c equating to 0.01 eV.

It can be seen that the optimization results of the two structures are quite similar. For the EMs propagating forward, the absorption rates are >0.1 in the range of 0.1–0.66 THz, and there is a trough and peak, with strong oscillation. Then in 0.66–3 THz, the absorption rate is lower than 0.1, and the absorption curve remains flat, in that the EMs propagating forward first pass through the periodic structure composed of materials

Table 1
Absorption for different N values at normal incidence.

N	Quasi-periodic sequences	AB	RBW	Absorption spectrum	ε_a	d_a (μm)	d_b (μm)	ε_c	d_c (μm)	μ_c (eV)
1	Thu_6	7.5 THz	127.12 %	2.15–9.65 THz	12.210	0.314	12.041	100	1.217	0.134
2		7.45 THz	122.63 %	2.35–9.8 THz	97.836	1.194	13.596	1.035	13.334	0.169
3		7.5 THz	121.95 %	2.4–9.9 THz	1.2195	1.2195	1.2195	1.2195	1.2195	1.2195
4		7.5 THz	121.95 %	2.4–9.9 THz	1	11.631	11.861	98.924	1.306	0.132
5		7.4 THz	120.97 %	2.5–9.9 THz	1	11.609	11.777	99.253	1.29	0.1325
1	Oct_6	7.6 THz	122.58 %	2.4–10 THz	90.283	0.188	7.844	100	1.055	0.0987
2		7.82 THz	129.04 %	2.15–9.97THz	99.47	1.29	9.50	1	12.05	0.0703
3		7.69 THz	125.14 %	2.31–10 THz	1.022	12.19	10.132	100	1.235	0.075
4		7.63 THz	123.76 %	2.37–10 THz	1	12.373	10.931	100	1.217	0.073
5		7.6 THz	122.58 %	2.4–10 THz	1	12.1	10.363	100	1.233	0.087

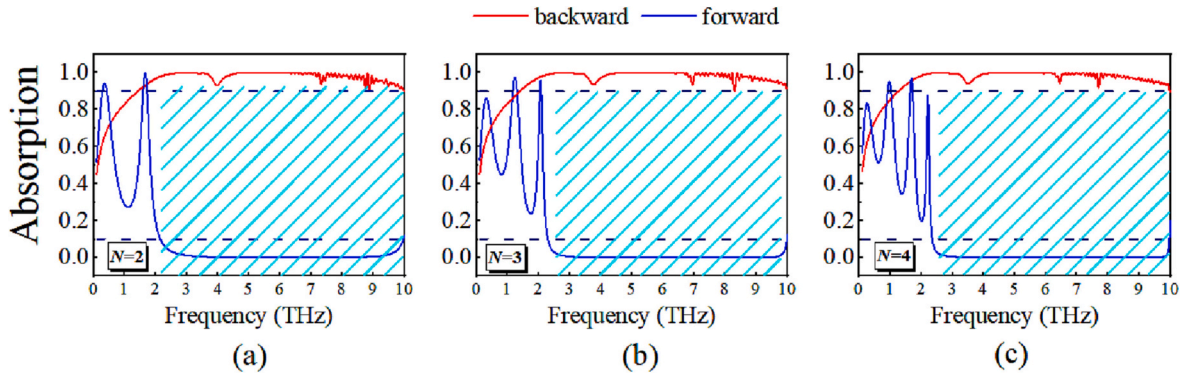

Fig. 3. The absorption spectra when the quasi-periodic sequence is Oct_6 with (a) $N = 2$, (b) $N = 3$, (c) $N = 4$.

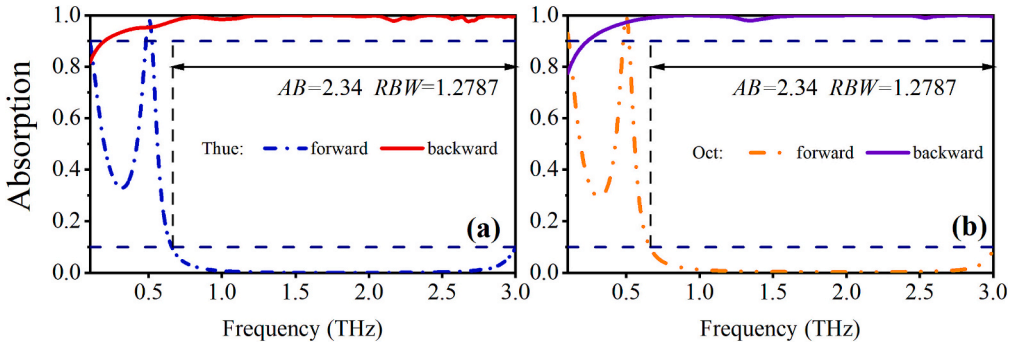

Fig. 4. The optimized absorptions with (a) Thu_6, (b) Oct_6 as the quasi-periodic structure respectively in 0.1–3 THz.

A and C, and the huge difference in refractive index between A and C leads to a large amount of reflection of EMs, and the absorption rate is close to 0. For the EMs propagating backward, the absorption curve is mostly stable above 0.9, close to 1, because the EMs first pass through the quasi-periodic sequence composed of air and graphene layer. And with the surface current of the graphene layer excited, the energy of the

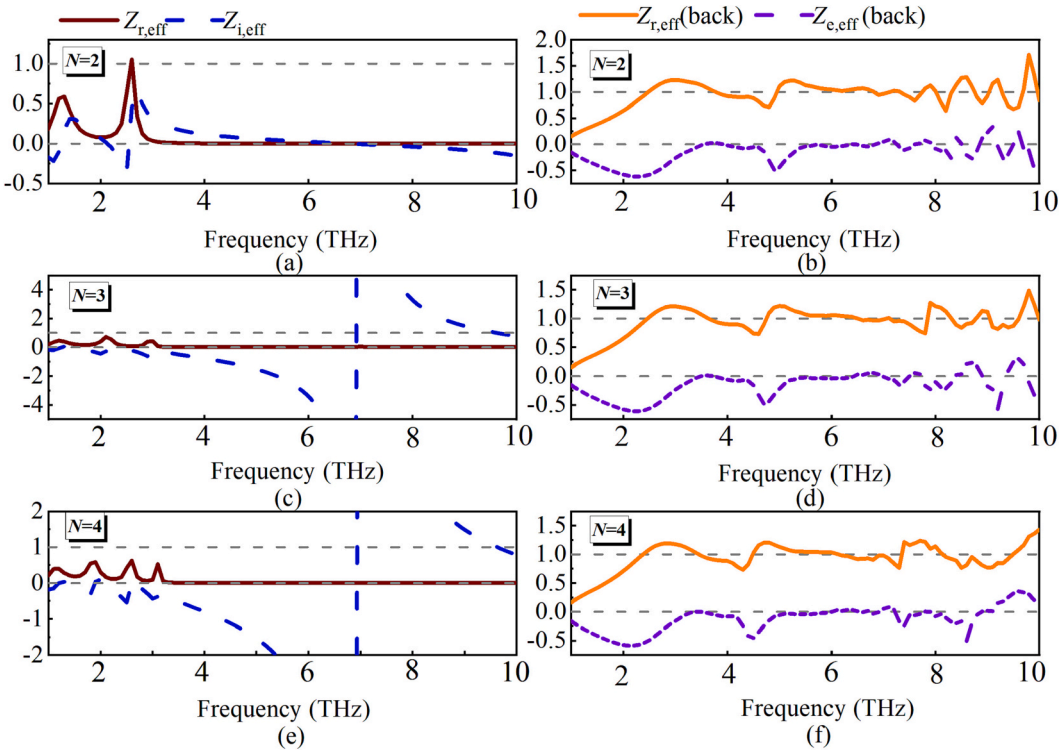

Fig. 5. The impedance matching spectra for the forward propagation are in (a), (c) and (e), and those for the reverse propagation are in (b), (d) and (f), with (a) (b) $N = 2$, (c) (d) $N = 3$, and (e) (f) $N = 4$.

EMs is limited in the graphene layer, bringing a perfect absorption effect. The *AB* of the two structures reaches 2.34 THz, and the *RBW* is as high as 127.87 %, realizing perfect non-reciprocal ultra-wide bandwidth absorption, which is due to the excellent impedance matching effect, and the absorption effect is optimized by the powerful parameter optimization ability of CGWO.

The perfect absorption can be attributed to a decent impedance match between the LSP and the free space. The normalized surface impedance can be calculated in Eq. (20)

$$\frac{Z_{eff}}{Z_0} = z_{r,eff} + jz_{i,eff} = \frac{1+r}{1-r} \tag{20}$$

where Z_{eff} is the effective surface impedance, and Z_0 represents the impedance of the wave in a vacuum. When normalized surface impedance is close to 1, which means $Z_{r,eff}$ is nearly 1, and $Z_{i,eff}$ is nearly 0, an impedance match is perfectly achieved, with the reflectivity r being close to 0, generating decent absorption of energy.

In the case of $N = 2$, 3, and 4, with Oct_6 as the quasi-period sequence, the spectra of impedance match are shown in Fig. 5.

In Fig. 5, the plots for (b), (d), and (f) show that, for the EMs in reverse propagation, the normalized surface impedance in 2.5–10 THz is approximately equal to 1 in the real part, and mainly around 0 in the imaginary part, resulting in significant absorption. However, the impedance in 0.1–2.5 THz does not obey this pattern, corresponding to poorer absorption.

For forward propagation, this pattern is not observed in the 0.1–10 THz. In Fig. 5(a), (c), and (e), the spline of $Z_{r,eff}$ is close to 0 from 2.5 THz to 10 THz and deviates from 1 in the 0.1–2.5 THz. Moreover, the spline of $Z_{i,eff}$ does not approach 0 in the most region within 0.1–10 THz, resulting in extremely low absorption. These observations confirm the correctness of the explanation of the impedance matching principle.

The study of the electric field distribution is helpful in further describing the physical mechanism of absorption. The electric field distribution of the LPS, is presented in Fig. 6, at 8 THz, with $N = 2$ and deploying the Oct_6 as the quasi-periodic sequence. The sequence of $\{\{AGC\}^N\text{-}Oct_6\}$ is expanded from left to right. In Fig. 6(a), when the EMs are incident along the negative direction of the *z*-axis, the electric field is concentrated on the right side of the proposed LPS, specifically in the Oct6 region composed of graphene and air layers. This strong electric resonance effectively shortens the current loop within the lossy medium, leading to enhanced absorption. When the diffusion of the EMs is in the forward direction, as shown in Fig. 6(b), the electric field is predominantly concentrated in the periodic sequence on the left side of the LPS, while the overall electric field in Oct_6 is weak, which is attributed to the potent reflection by the $\{AGC\}^N$ periodic sequence, preventing the energy from reaching the Oct_6.

3.1.2. The effect of M on the AB

The impact of *M* on the bandwidth is a crucial factor to consider. In that *N* has a negligible effect on bandwidth, assuming $N = 2$ for brevity, and considering vertical incidence, with $T = 300$ K, the Thue-morse and Octonacci sequences have values of *M* that are 4, 5, and 6, respectively.

Table 2
The relative optimized parameters of Fig. 7.

M	The quasi-period sequence	ε_a	d_a (μm)	d_b (μm)	ε_c	d_c (μm)	μ_c (eV)
4	Octonacci	92.927	56.792	19.615	95.787	98.337	0.197
5		87.632	1.370	12.715	1.222	11.395	0.211
6		99.480	1.292	9.5001	1.000	12.053	0.070
4	Thue-morse	74.334	0.996	7.855	1.819	8.176	0.298
5		1.955	5.74	6.438	80.670	0.864	0.244
6		97.836	1.194	13.596	1.035	13.334	0.169

Table 2 displays the optimized parameters, while the absorption diagram is depicted in Fig. 7.The absorption diagrams for reverse propagating EMs are displayed above, while those for forward propagation are below.

In Fig. 7, a strong positive correlation between *M* and *AB* can be observed, which stems from an increase in the number of resonance structures. The absorption curve for the Octonacci sequence as the quasi-sequence is shown in Fig. 7(a). As *M* increases from 4 to 6, the upper cutoff frequency of the absorption curve in the reverse propagation undergoes a blue shift, changing from 8.7 THz to 10 THz, accompanied by a decrease in the oscillation of the curve in the 6–10 THz. The lower cutoff frequency also undergoes a redshift. However, a trough between 3 and 5 THz is consistently present and red-shifted as *M* increases. For the forward wave, the curves between 3 and 10 THz remain flat and close to zero. In the 0.1–3 THz, the lower cutoff frequency shifts from 2.9 THz to 2.3 THz as *M* increases, while the positions of both peaks and valley points in this band are gradually red-shifted, with the amplitude gradually magnified.

In general, owning to the increase of *M*, the number of resonant structures is greatly aggrandized, which brings a better impedance matching, resulting in an increase of *AB* from 5.8 THz to 7.82 THz and lifting *RBW* from 100 % to 129.04 %.

By utilizing the Thue-Morse sequence as a quasi-periodic sequence (as shown in Fig. 7(b) with $M = 4$, the absorption of the forward propagation waves exhibits two peaks at 0.9 THz and 2.7 THz, respectively, while that of the EMs in reverse propagation displays a low absorption rate ranging from 0.1 THz to 4.25 THz, which results in the formation of a narrow, ideal non-reciprocal absorption region between 4.25 THz and 8.25 THz, with an *AB* of 4 THz and an *RBW* of 63.28 %. As the number of layers in the graphene film structure increases with *M*, the optimization of the algorithm is further enhanced, resulting in a blue shift of the upper cutoff frequency and a redshift of the lower cutoff frequencies, respectively. This leads to a greater *AB* and *RBW*. For instance, when $M = 5$, the ideal absorption region expands to 2.7–9.1 THz, with corresponding *AB* = 5.4 THz and *RBW* = 74.91 %. When $M = 6$, the optimized ideal interval ranges from 2.35 THz to 9.8 THz, and the *RBW* is 122.63 %. The continuous improvement in the absorption effect can be attributed to the gradual amplification of the optimization gain facilitated by the CGWO with an increase in the number of media layers, resulting in a better impedance-matching effect. Notably, despite the varying value of *M*, the

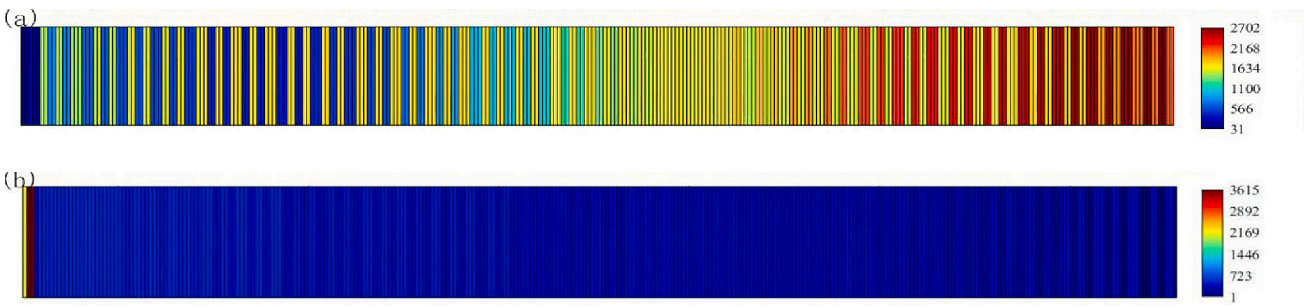

Fig. 6. The dispersion of electric field in the LPS at 8 THz, for the EMs propagating alone (a) the positive direction of *z*-axis (b) the opposite direction.

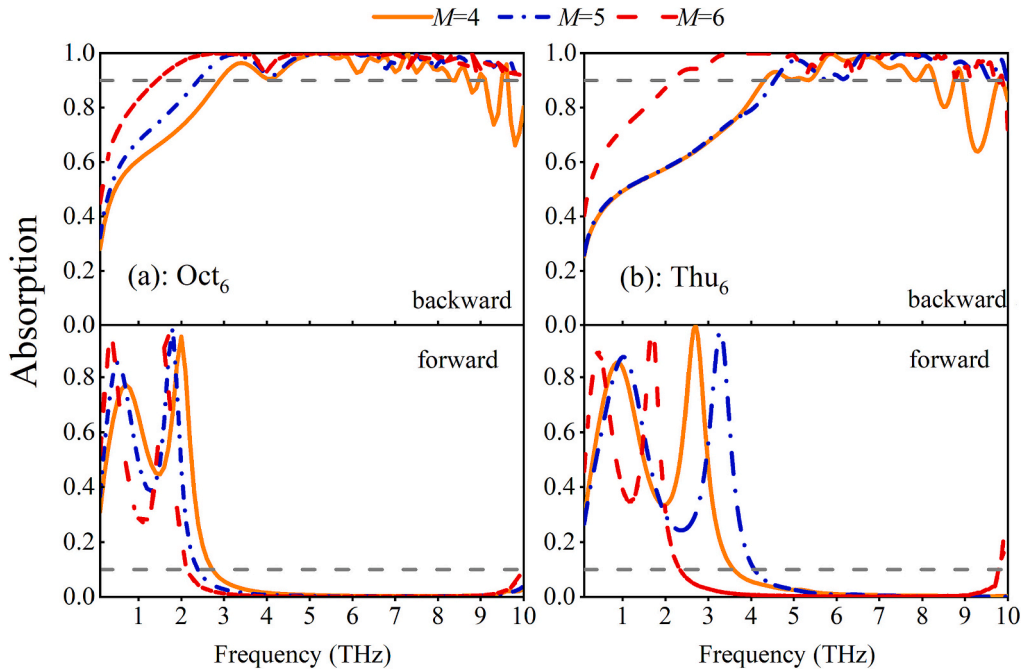

Fig. 7. The optimization results of taking different values of *M* when (a) Octonacci sequence, (b) Thue-morse sequence are respectively used as quasi-periodic sequences.

RBW remains above 63 %, attesting to the superior absorption performance of the structure under the assistance of optimization algorithms.

Furthermore, as the value of parameter *M* increases, the optimization outcomes of the two sequences become more similar. In contrast, when *M* is small, the Octonacci sequence exhibits significantly better performance than the Thue-morse sequence. These findings suggest that an increase in the number of layers can further obscure the differences in superiority between the two structures.

3.2. Angle-insensitive and non-reciprocal absorption

3.2.1. The specific results

Graphene holds tremendous potential for achieving angular stability in structures. To investigate the probability of non-reciprocal and angular-insensitive absorption, the CGWO method is utilized. The optimization task now becomes a dual-objective optimization, with the objective functions being bandwidth and angular stability.

Moreover, as there exists a positive correlation between the value of *M* and *AB*, set *M* to 6. In that the effect of *N* on bandwidth is negligible when *M* is 6, *N* is taken to 2 during the optimization.

Finally, six different sets of non-reciprocal and high-angle absorption results for the two structures are obtained, due to the differences in the frequency band, bandwidth, and angular stability. The specific results and optimized parameters are presented in Table 3.

Herein, the absorption of forward-propagating EMs is defined as *A*, and that of backward-propagating EMs as *oppA*. To quantify the difference in absorption rates, the isolation degree *S* is introduced, which is defined as $S = oppA\text{-}A$. Based on the findings, posit that $S > 0.8$ represents an ideal condition for unidirectional absorption, where the absorption of backward-propagating EMs, *oppA*, should exceed 0.9 and that of forward-propagating EMs, *A*, should be <0.1.

Table 3 reveals that the angular stability under the TM mode outperforms that under the TE mode in terms of efficacy, with the former achieving a high degree of over 80° in most cases, and up to 87°, while the latter only reaches a maximum of 70°. Notably, a clear trend emerges in which the diminution of the frequency range, for the same sequence, results in improved angular stability performance, particularly under the TE mode. For example, As the *AB* increases from 3 THz to 5 THz, the angular stability under the TE mode reduces from 70° to 60°, and under the TM mode, it decreases from roughly 85° to 80°. Hence, it is possible to tailor the degree of importance assigned to angular stability and bandwidth size by modifying relevant parameters in the objective function, thereby achieving the desired effect.

To simplify the presentation of the absorption results, only cases 2 and 5 are shown in Fig. 8. In this plot, a negative incidence angle corresponds to the TE polarization mode, while a positive angle represents the TM mode. The absorption results of the back propagating EMs are shown in Fig. 8(a) and (c), with the ideal region having an absorption rate >0.9 being enclosed by a blue solid line. On the other hand, the absorption effects of the forward propagating EMs are displayed in Fig. 8 (b) and (d). The ideal region is separated by a white line, within which the absorption rate remains below 0.1. The overlapping region of these two areas represents the expected non-reciprocal absorption region.

Taking the Thu_6 as the quasi-periodic sequence, with the optimized region of 2–5 THz, the absorption results of backward propagation and forward propagation are displayed in Fig. 8(a) and Fig. 8(b),

Table 3
Results of optimization for non-reciprocal angle stability and the relative parameters.

Structure	Optimized scope	*RBW*	Angular stability		Case number	ε_a	d_a (μm)	d_b (μm)	ε_c	d_c (μm)	μ_c (eV)
Thu_6	3–8 THz	90.9 %	TE: 60°	TM: 80°	1	2.154	9.653	15.629	99.784	1.498	0.132247
	2–5 THz	85.7 %	TE: 70°	TM: 84°	2	98.931	2.396	29.16	2.14	15.569	0.10063
	2–7 THz	110 %	TE: 65°	TM: 70°	3	100	1.705	19.282	1.885	12.859	0.110898
Oct_6	3–8 THz	89.9 %	TE: 60°	TM: 80°	4	100	1.443	14.836	2.365	9.8	0.10553
	1.5–4.5 THz	100 %	TE: 70°	TM: 86°	5	2.11	18.714	32.406	99.352	2.576	0.100
	2–5.9 THz	98 %	TE: 65°	TM: 87°	6	99.104	1.952	24.851	2.458	12.748	0.101

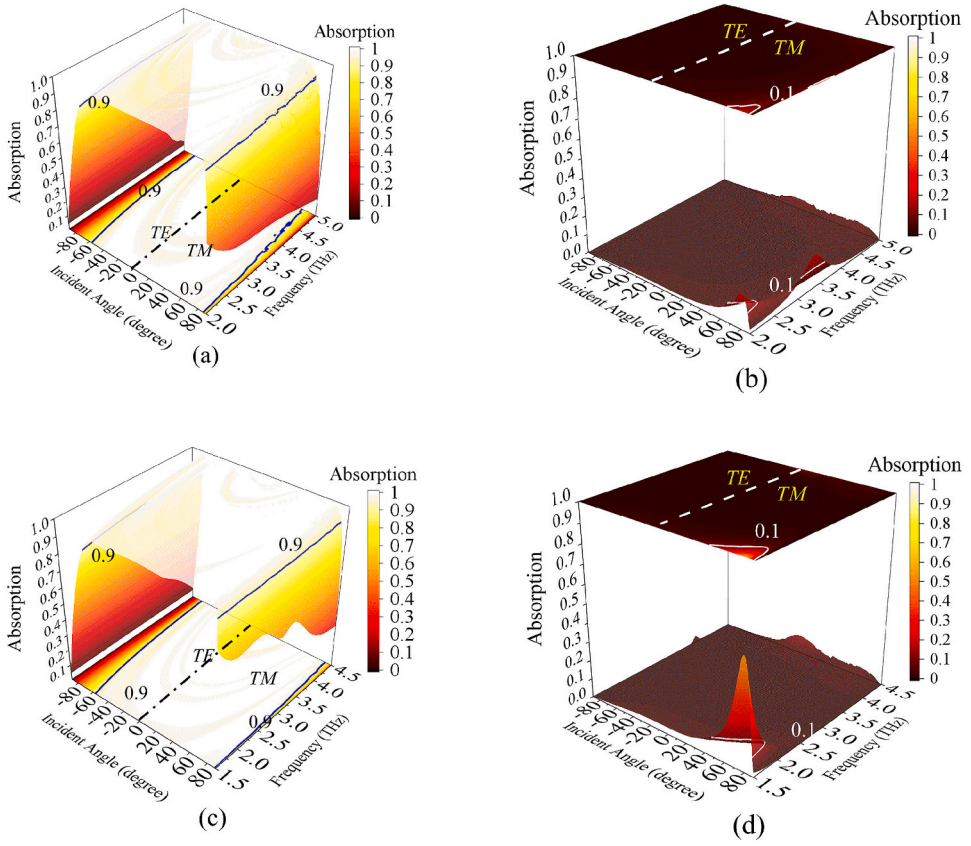

Fig. 8. Large-angle non-reciprocal absorption profiles corresponding to the conditions in cases 2, and 5. (a)(b) denote case 2, (c)(d) present case 5.

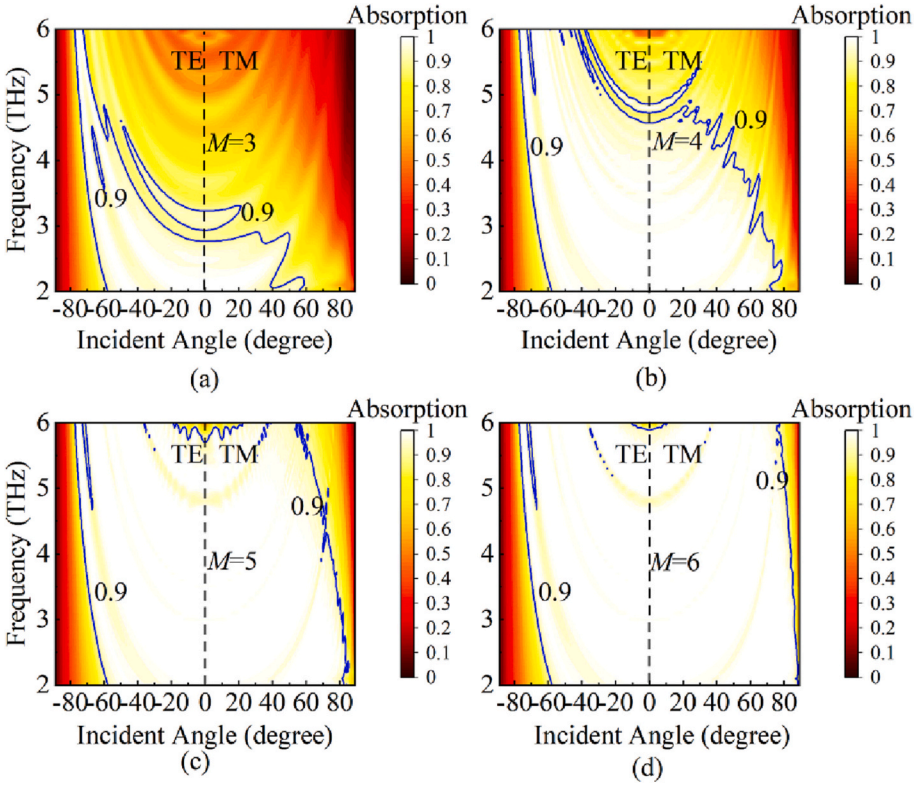

Fig. 9. Absorption effect profiles with M taken to (a) $M = 3$, (b) $M = 4$, (c) $M = 5$, (d) $M = 6$.

respectively. The ideal non-reciprocal absorption region is represented by the overlapping section inside of the white solid lines in both figures. The unidirectional absorption bandwidth is 3 THz, with a *RBW* of 85.7 %, and the angle maximum is 70° under the TE mode and 84° under the TM mode. In Fig. 8(b), the area of the ideal region (where the absorption rate is <0.1) is extensive, and only the region with high incidence angles in the 1.5–2.5 THz under TM mode does not meet the condition. This implies that the nonreciprocal large-angle absorption region is determined by the absorption during backward propagation. As depicted in Fig. 8(a), under the TM mode, most areas with incident angles lower than 84° exhibit absorption rates >0.9, while under the TE mode, only areas below 70° satisfy the rule. Furthermore, all defects within the ideal areas are optimized.

Likewise, when the Oct_6 serves as the quasi-periodic sequence, a similar outcome is achieved within 1.5 to 4.5 THz. As shown in Fig. 8(d), the region where the absorption is below 0.1 is roomy, with only the high angle incidence component within 1.5–2.5 THz failing to meet the criteria. Therefore, the nonreciprocal absorption region is determined by the absorption during the backward propagation of EMs. Under the TM mode, the angle maximum is as high as 86° in Fig. 8(c), whereas, for the TE waves, it is only 70°, that for TE waves, as the frequency decreases, the regions with high incidence angles fail to satisfy impedance matching, resulting in absorption rates below 0.9. Lastly, the absorption bandwidth is 3 THz, with a *RBW* of 100 %, and the angle maximum is 70° under the TE mode and 86° under the TM mode.

3.2.2. Effect of *M* on angular stability

As the influence of *N* is weakened by *M*, the focus here is solely on the impact of *M* on the angle stability. While keeping the other conditions of the 6th case in Table 3 constant, the values of *M* range from 3 to 6. The absorption of the waves propagating in the opposite direction is depicted in Fig. 9.

The blue solid line in Fig. 9 represents the ideal absorption region, which is the portion where the absorption is above 0.9. At $M = 3$, the maximum continuous *AB* is only 0.8 THz, with angular stability reaching 56° under the TE mode and 36° under the TM mode. However, when *M* is raised to 4, the high absorption region expands swiftly. The maximum absorption angle for the TE waves reaches 60°, while that under the TM mode reaches 58°. Simultaneously, the bandwidth expands to 2.6 THz.

Upon raising *M* to 5, the ideal absorption region expands further, and the maximum incidence angle reaches 65° under the TE mode and nearly 70° under the TM mode. The absorption rate in the 4–6 THz with the 40–60° incident angle region improves to >0.9. Additionally, the absorption bandwidth is further improved, with *AB* reaching 3.68 THz and *RBW* measuring 98.5 %. Finally, at $M = 6$, *RBW* reaches 98 %, and the absorption area expands to 65° under the TE mode and 87° under the TM mode. To sum up, it is evident that both the bandwidth and wide-angle absorption are amplified with increasing values of *M*.

3.3. Impacts of μ_c

3.3.1. Effect of μ_c on the AB of the nonreciprocal absorption

To investigate the impact of the chemical potential on broadband absorption at normal incidence, the Fermi level is incrementally raised from 0.1 eV to 1 eV, with *N* is 2, and taking Oct_6 as the quasi-period sequence. The optimized results and the relative parameters are summarized in Table 3.

A clear negative correlation between the Fermi level and the absorption bandwidth is demonstrated in Table 4. Notably, when μ_c is set to 0.1 eV, the maximum *AB* value reaches 7.78 THz, with a corresponding *RBW* value of 127.33 %. It is worth noting that the *AB* remains consistently high, ranging from 7.13 THz to 7.78 THz, while the *RBW* remains above 110 %, for μ_c ranging from 0.1 eV to 0.3 eV. As μ_c increases from 0.4 eV to 0.6 eV, *AB* gradually decreases from 5.53 THz to 4.68 THz, and *RBW* decreases rapidly from 94.45 % to 66.7 %, before stabilizing at 61.5 %. Between 0.7 eV and 1 eV, *AB* remains stable at approximately 2.5THz, with a *RBW* ranging from 26.4 % to 32.42 %. At $\mu_c = 1$ eV, *AB* reaches a minimum of 2.33 THz and *RBW* reaches a minimum of 26.4 %, which still exceeds the threshold of 25 % for ultra-wide bandwidth absorption. The corresponding absorption curves for μ_c from 0.1 eV to 1 eV are presented in Fig. 10.

As depicted in Fig. 10(a), the absorption curve of the back-propagating EMs exhibits an improvement in oscillation amplitude in the high-frequency band as μ_c is elevated. Moreover, the number of troughs and peaks ascends, as well as a gradual redshift of the upper cutoff frequency (at $A = 0.9$). In contrast, the lower cutoff frequency undergoes a persistent blue shift, particularly during μ_c transiting from 0.3 eV to 0.4 eV, resulting in a sharp decrease of *AB* from 7.13 THz to 5.53 THz. In Fig. 10(b), the absorption curve of forward propagating EMs displays a stable absorption rate below 0.1 in the high-frequency range as μ_c rises. At the same time, the number of wave peaks in the low-frequency range remains at 2, but the lower cutoff frequency (at $A = 0.1$) continues to blue shift. Markedly, a significant blue shift occurs during the transition of μ_c from 0.6 eV to 0.7 eV, resulting in a rapid decline of *AB* from 4.68 THz to 2.79 THz, while *RBW* decreases from 61.5 % to 32.42 %.

Due to the negative correlation between chemical potential and bandwidth, for all the ultra-wide bandwidth absorption effects obtained in this paper, the corresponding chemical potentials are between 0.001 eV and 0.3 eV.

3.3.2. Effect of μ_c on angular stability

To investigate how the chemical potential μ_c affects angular stability, values of μ_c are varied from 0.1 eV to 0.7 eV in ascending order, based on the fifth case conditions in Table 5. The corresponding large-angle absorption profiles are presented in Fig. 11.

As depicted in the figure, the absorption effect is poorest when μ_c is 0.7 eV, with the portion satisfying the criterion ($A > 0.9$) mainly concentrated in the 30–89° range of incidence angle in the TM mode at 3–4.5 THz, exhibiting a weaker absorption effect under the TE mode, and the *AB* at vertical incidence is only 0.3 THz. When μ_c is 0.5 eV, the

Table 4
The comparison of absorption when μ_c are taken to different values.

μ_c (eV)	*AB*	*RBW*	ε_a	d_a (μm)	d_b (μm)	ε_c	d_c (μm)
0.1	7.78 THz	127.33 %	1.000	12.394	10.915	100	1.254
0.2	7.63 THz	123.36 %	100.000	1.268	11.195	1.000	11.860
0.3	7.13 THz	110.80 %	1.000	10.756	11.987	100.000	1.150
0.4	5.53 THz	94.45 %	1.258	8.442	14.046	73.742	1.519
0.5	5 THz	66.70 %	2.836	5.285	12.12	94.629	1.102
0.6	4.68 THz	61.50 %	97.539	0.747	12.258	1.222	7.544
0.7	2.79 THz	32.42 %	87.913	0.376	12.292	2.481	7.77
0.8	2.62 THz	30.18 %	1.515	5.820	12.397	45.461	1.225
0.9	2.47 THz	28.21 %	39.314	1.487	12.481	1.239	3.792
1	2.33 THz	26.40 %	44.213	1.546	12.553	1.000	6.535

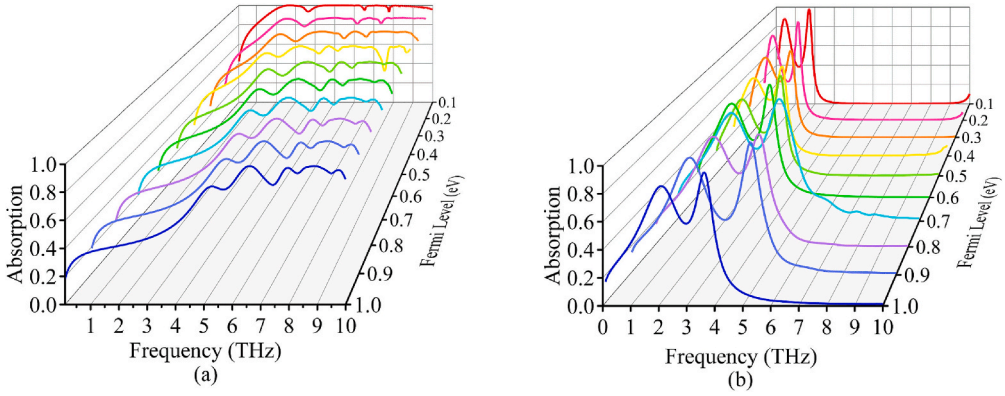

Fig. 10. Absorption curves of different values of chemical potential for the EMs in (a) the reverse propagation, (b) the forward propagation.

Table 5
Comparison of the performance of different terahertz absorbers.

Reference	Operating band (A > 0.9)	*AB*	RBW	Angular insensitivity (A > 0.9)		Having non-reciprocity?
				TE mode	TM mode	
[34]	6.39–9.47 THz	3.08 THz	38.8 %	8°	8°	No
[35]	3.39–5.96 THz	2.57 THz	54.9 %	40°	40°	No
[36]	2.6–3.5 THz	0.9 THz	29.5 %	45°	45°	No
[37]	5.78–6.48 THz	0.7 THz	11.42 %	60	62	No
Our work	1.5–4.5 THz	3 THz	100 %	70°	86°	Yes

ideal absorption region in the TM mode extends to 2.7 THz, while the angle stability under the TE mode is limited to 40°. The *AB* increases to 1.4 THz, and the *RBW* reaches 45.1 %. As the Fermi level decreases, the absorption effect improves, and finally, when μ_c is 0.1 eV, the absorption effect of large-angle ultra-broadband achieves the best performance. A 100 % *RBW* is attained, while the angular stability reaches 86° under the TM mode and 70° under the TE mode.

This confirms the previous speculation that a smaller chemical potential results in a wider bandwidth. It is also observed that achieving angular stability is easier under the TM mode than under the TE mode. Generally, decreasing the chemical potential leads to better angular stability, with a more pronounced effect under the TE mode.

Finally, Table 5 provides an analysis of the differences between our current work and the existing THz absorbers. In comparison to previous achievements, our absorber demonstrates clear advantages in terms of bandwidth and angular stability. Additionally, it exhibits a rare non-reciprocal characteristic that is not commonly found in most absorbers.

Based on these findings, we firmly believe that the proposed ultra-

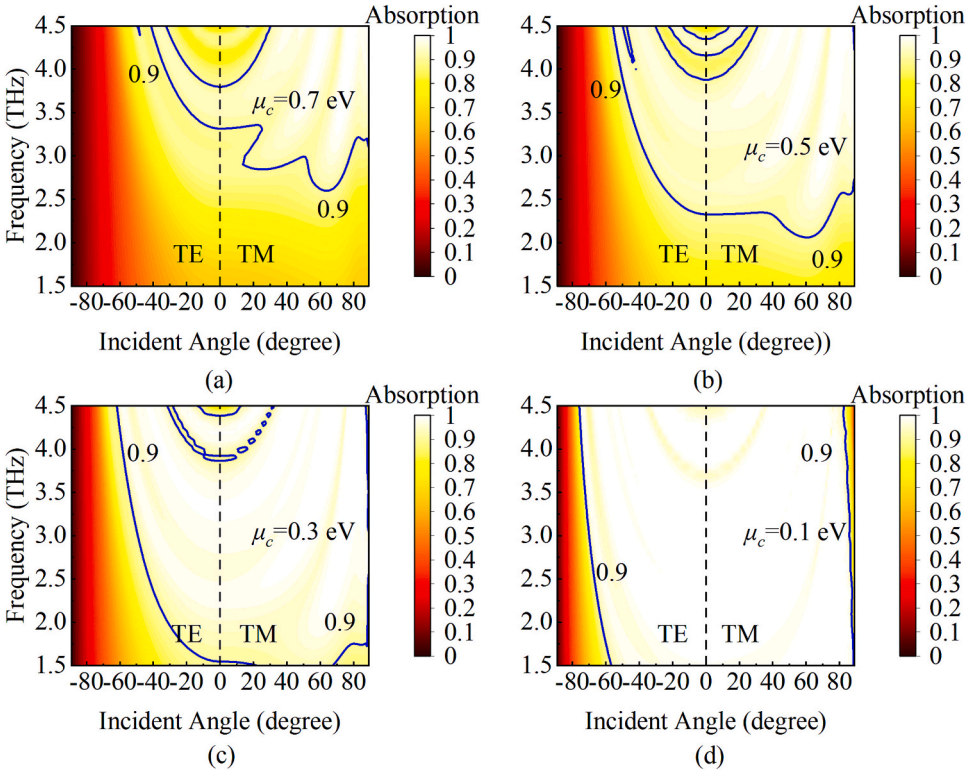

Fig. 11. Diagrams of absorptance for (a) μ_c = 0.7 eV, (b) μ_c = 0.5 eV, (c) μ_c = 0.3 eV, (d) μ_c = 0.1 eV.

wideband, angle-insensitive, and non-reciprocal absorber holds tremendous application potential in various fields, including military stealth, energy harvesting, and addressing electromagnetic wave pollution.

4. Conclusion

In summary, a nonreciprocal ultra-wide bandwidth structure with excellent angular insensibility is fulfilled, which is comprised of the periodic and quasi-periodic sequences, made of graphene-embedded LPS. The breaking of spatial symmetry and unique absorption properties of graphene led to the successful optimization of each parameter in CGWO, resulting in perfect unidirectional absorption across the 2.15–9.97 THz with a *RBW* of 129.04 %. Furthermore, in a specific band within 0.1–10 THz, the angular stability is achieved at 70° under the TE mode, and 86° under the TM mode, with a corresponding *RBW* of 100 %. The ultra-broadband absorption phenomenon is explained by the impedance matching principle. What is more, the impact of *N* and *M* on perfect absorption has been examined, revealing that *N* has only a minor effect on bandwidth when *M* is large, and its primary role is to enable non-reciprocity. As *M* increases, both the absorption bandwidth and angular stability improve, which is attributed to the rise in the number of resonance structures, and the effect remains steady after reaching a certain threshold. The effect of the Fermi level is also surveyed, and it is found that this parameter can significantly tune the entire absorption spectrum. Following optimization, the proposed structure showcases tremendous potential in addressing design challenges within the realm of optoelectronic devices. It offers promising solutions to a wide range of problems, including but not limited to EM wave pollution, military stealth applications, and advancements in solar cell technology. The CGWO algorithm can be widely applied in various optical fields, such as the design of optical absorbers, sensors, and communication systems, to improve their performance and efficiency.

CRediT authorship contribution statement

Zhao Tang: Data curation, Formal analysis, Investigation, Writing – original draft, Visualization. **Jie Xu:** Software, Validation. **Shuo Wang:** Software, Validation. **Hai-Feng Zhang:** Conceptualization, Methodology, Supervision, Writing – review & editing.

Declaration of competing interest

No conflict of interest exists in the submission of this manuscript, and the manuscript is approved by all authors for publication.

Data availability

Data will be made available on request.

References

[1] H. Chen, W. Ma, Z. Huang, Y. Zhang, Y. Huang, Y. Chen, Graphene-based materials toward microwave and terahertz absorbing stealth technologies, Adv. Opt. Mater. 7 (2019) 1801318, https://doi.org/10.1002/adom.201801318.

[2] Y. Wu, S. Tan, Y. Zhao, L. Liang, M. Zhou, G. Ji, Broadband multispectral compatible absorbers for radar, infrared and visible stealth application, Prog. Mater. Sci. (2023), 101088, https://doi.org/10.1016/j.pmatsci.2023.101088.

[3] A. Namai, S. Sakurai, M. Nakajima, T. Suemoto, K. Matsumoto, M. Goto, S. Sasaki, S.-I. Ohkoshi, Synthesis of an electromagnetic wave absorber for high-speed wireless communication, J. Am. Chem. Soc. 131 (2009) 1170–1173, https://doi.org/10.1021/ja807943v.

[4] A. Ren, A. Zahid, D. Fan, X. Yang, M.A. Imran, A. AlomainyQ, H. Abbasi, State-of-the-art in terahertz sensing for food and water security–a comprehensive review, Trends Food Sci. Technol. 85 (2019) 241–251, https://doi.org/10.1016/j.tifs.2019.01.019.

[5] R. Knipper, A. Brahm, E. Heinz, T. May, G. Notni, H.-G. Meyer, A. Tünnermann, J. Popp, THz absorption in fabric and its impact on body scanning for security application, IEEE Trans Terahertz. Technol. 5 (2015) 999–1004, https://doi.org/10.1109/TTHZ.2015.2474115.

[6] M. Baqir, P.K. Choudhury, Hyperbolic metamaterial-based UV absorber, IEEE Photon. Technol. Lett. 29 (2017) 1548–1551, https://doi.org/10.1109/LPT.2017.2735453.

[7] M.A. Baqir, Conductive metal–oxide-based tunable, wideband, and wide-angle metamaterial absorbers operating in the near-infrared and short-wavelength infrared regions, Appl. Opt. 59 (2020) 10912–10919, https://doi.org/10.1364/AO.411268.

[8] M.A. Naveed, R.M.H. Bilal, A.A. Rahim, M.A. BaqirM, M. Ali, Polarization-insensitive dual-wideband fractal meta-absorber for terahertz applications, Appl. Opt. 60 (2021) 9160–9166, https://doi.org/10.1364/AO.438237.

[9] A.K. Geim, Graphene: status and prospects, Science 324 (2009) 1530–1534, https://doi.org/10.1126/science.115887.

[10] A. Martinez, Z. Sun, Nanotube and graphene saturable absorbers for fibre lasers, Nat. Photonics 7 (2013) 842–845, https://doi.org/10.1038/nphoton.2013.304.

[11] Baylam Isnsu, Ozharar Sarper, Kakenov Nurbek, Kocabas Coskun, Alphan Sennaroglu, Femtosecond pulse generation from a Ti^{3+}: sapphire laser near 800nm with voltage reconfigurable graphene saturable absorbers, Opt. Lett. 42 (2017) 1404, https://doi.org/10.1364/OL.42.001404.

[12] J. Nagi, S. Jana, Operating regimes of cavity solitons by virtue of a graphene flake saturable absorber, Phys. Rev. E 104 (2021), 024209, https://doi.org/10.1103/PhysRevE.104.024209.

[13] N. Kakenov, T. Takan, V.A. Ozkan, O. Balcı, E.O. Polat, H. Altan, C. Kocabas, Graphene-enabled electrically controlled terahertz spatial light modulators, Opt. Lett. 40 (2015) 1984–1987, https://doi.org/10.1364/OL.40.001984.

[14] S. Bae, H. Kim, Y. Lee, X. Xu, J.S. Park, Y. Zheng, J. Balakrishnan, T. Lei, H. R. KimY, I. Song, Roll-to-roll production of 30-inch graphene films for transparent electrodes, Nat. Nanotechnol. 5 (2010) 574–578, https://doi.org/10.1038/nnano.2010.132.

[15] K.S. Kim, Y. Zhao, H. Jang, S.Y. Lee, J.M. Kim, K.S. Kim, J.-H. Ahn, P. Kim, J.-Y. ChoiB, H. Hong, Large-scale pattern growth of graphene films for stretchable transparent electrodes, Nature 457 (2009) 706–710, https://doi.org/10.1038/nature07719.

[16] A. Chambel, A.L. Sanati, P.A. Lopes, T. Nikitin, R. Fausto, A.T. de Almeida, M. Tavakoli, Laser writing of eutectic gallium–indium alloy graphene-oxide electrodes and semitransparent conductors, Adv. Mater. Technol. 7 (2022) 2101238, https://doi.org/10.1002/admt.202101238.

[17] Z. Yin, J. Zhu, Q. He, X. Cao, C. Tan, H. Chen, Q. Yan, H. Zhang, Graphene-based materials for solar cell applications, Adv. Energy Mater. 4 (2014) 1300574, https://doi.org/10.1002/aenm.201300574.

[18] Y. Areerob, C. Hamontree, P. Sricharoen, N. Limchoowong, S. Laksee, W.-C. Oh, K. Pattarith, Novel gamma-irradiated chitosan-doped reduced graphene-$CuInS_2$ composites as counter electrodes for dye-sensitized solar cells, RSC Adv. 12 (2022) 15427–15434, https://doi.org/10.1039/D2RA01749K.

[19] R.R. Nair, P. Blake, A.N. Grigorenko, K.S. Novoselov, T.J. Booth, T. Stauber, N. M. PeresA, K. Geim, Fine structure constant defines visual transparency of graphene, Science 320 (2008) 1308, https://doi.org/10.1126/science.11569.

[20] X. Wang, Y. Liang, L. Wu, J. Guo, X. Dai, Y. Xiang, Multi-channel perfect absorber based on a one-dimensional topological photonic crystal heterostructure with graphene, Opt. Lett. 43 (2018) 4256–4259, https://doi.org/10.1364/OL.43.004256.

[21] J. Wu, Multichannel absorption enhancement in graphene based on metal-photonic crystal hetero-structure, ES Energy Environ. 13 (2021) 25–30, https://doi.org/10.30919/esee8c471.

[22] J. Wu, TPP-assisted multi-band absorption enhancement in graphene based on Fibonacci quasiperiodic photonic crystal, Results Phys. 33 (2022), 105210, https://doi.org/10.30919/esee8c471.

[23] B. Roumi, R. Abdi-Ghaleh, H. Akkus, Single-frequency into dual-frequency absorption switch based on a one-dimensional photonic crystal containing graphene and vanadium dioxide layers, Photonic. Nanostruct. 53 (2023), 101111, https://doi.org/10.1016/j.photonics.2023.101111.

[24] S. He, T. Chen, Broadband THz absorbers with graphene-based anisotropic metamaterial films, IEEE Trans. Terahertz Sci. 3 (2013) 757–763, https://doi.org/10.1109/TTHZ.2013.2283370.

[25] M. Vincenti, D. De Ceglia, M. Grande, A. D'Orazio, M. Scalora, Nonlinear control of absorption in one-dimensional photonic crystal with graphene-based defect, Opt. Lett. 38 (2013) 3550–3553, https://doi.org/10.1364/OL.38.003550.

[26] P. Cao, X. Yang, S. Wang, Y. Huang, N. Wang, D. DengC, T. Liu, Ultrastrong graphene absorption induced by one-dimensional parity-time symmetric photonic crystal, IEEE Photon. J. 9 (2017) 1–9, https://doi.org/10.1109/JPHOT.2017.2653621.

[27] L.-A. Bian, P. Liu, G. Li, Design of tunable devices using one-dimensional Fibonacci photonic crystals incorporating graphene at terahertz frequencies, Superlattice. Microst. 98 (2016) 522–534, https://doi.org/10.1016/j.spmi.2016.08.029.

[28] S. Mirjalili, S.M. Mirjalili, A. Lewis, Grey wolf optimizer, Adv. Eng. Softw. 69 (2014) 46–61, https://doi.org/10.1016/j.advengsoft.2013.12.007.

[29] T. Zhan, X. Shi, Y. Dai, X. Liu, J. Zi, Transfer matrix method for optics in graphene layers, J. Phys. Condens. Matter 25 (2013), 215301, https://doi.org/10.1088/0953-8984/25/21/215301.

[30] E. Brandão, C. Costa, M. Vasconcelos, D. Anselmo, V. Mello, Octonacci photonic quasicrystals, Opt. Mater. 46 (2015) 378–383, https://doi.org/10.1016/j.optmat.2015.04.051.

[31] N.-H. Liu, Propagation of light waves in Thue-Morse dielectric multilayers, Phys. Rev. B 55 (1997) 3543, https://doi.org/10.1103/PhysRevB.55.3543.

[32] S.A. Mikhailov, K. Ziegler, New electromagnetic mode in graphene, Phys. Rev. Lett. 99 (2007), 016803, https://doi.org/10.1103/PhysRevLett.99.016803.

[33] A. Andryieuski, A.V. Lavrinenko, Graphene metamaterials based tunable terahertz absorber: effective surface conductivity approach, Opt. Express 21 (2013) 9144–9155, https://doi.org/10.1364/OE.21.009144.
[34] H.-B. Liu, C.-X. Hu, Z.-L. Wang, H.-F. Zhang, H.-M. Li, An ultra-wideband terahertz metamaterial absorber based on the fractal structure, Plasmonics 16 (2021) 263–271, https://doi.org/10.1007/s11468-020-01288-3.
[35] J.-Z. Sun, J.-S. Li, Broadband adjustable terahertz absorption in series asymmetric oval-shaped graphene pattern, Front. Phys. 8 (2020) 245, https://doi.org/10.3389/fphy.2020.00245.
[36] A. Mohanty, O.P. Acharya, B. Appasani, S. Mohapatra, A broadband polarization insensitive metamaterial absorber using petal-shaped structure, Plasmonics 15 (2020) 2147–2152, https://doi.org/10.1007/s11468-020-01241-4.
[37] Y. Cai, K.-D. Xu, Tunable broadband terahertz absorber based on multilayer graphene-sandwiched plasmonic structure, Opt. Express 26 (2018) 31693–31705, https://doi.org/10.1364/OE.26.031693.